

1 Nano-scale earthquake records preserved in plagioclase 2 microfractures from the lower continental crust

3 Petley-Ragan, A.^{1*}, Plümer, O.², Ildefonse, B.³ and Jamtveit, B.¹

4 ¹Physics of Geological Processes, The Njord Centre, University of Oslo, Oslo, Norway

5 ²Department of Earth Sciences, Utrecht University, Utrecht, The Netherlands

6 ³Géosciences Montpellier, CNRS, University of Montpellier, Université des Antilles, Montpellier, France

7 *Corresponding to: Arianne J. Petley-Ragan (a.j.petley-ragan@geo.uio.no)

8 **Abstract.** Seismic faulting causes wall rock damage driven by both mechanical ~~stress and thermal energy and~~
9 ~~thermal stress~~. In the lower crust, co-seismic damage ~~has important implications [MOU1]for increases~~ wall rock
10 permeability, ~~the progress of~~permits fluid infiltration and triggers ~~subsequent fluid driven~~ metamorphic reactions,
11 ~~and that transforms~~ rock rheology. Wall rock microstructures reveal high-stress conditions near ~~the slip~~
12 ~~surface earthquake faults during lower crustal earthquakes~~, however, there is limited documentation on the ~~thermal~~
13 ~~effects of a thermal pulse coupled with fluid infiltration~~. Here, we present a transmission electron microscopy
14 study of co-seismic microfractures in plagioclase feldspar from lower crustal granulites from the Bergen Arcs,
15 Western Norway. Focused ion beam foils are collected 1.25 mm and 1.8 cm from a ~~2-1.3~~ mm thick eclogite facies
16 pseudotachylyte vein. Dislocation-free plagioclase ~~and K-feldspar~~ aggregates fill the microfractures and record a
17 history of ~~fluid introduction and~~ recovery from a short-lived high stress ~~high temperature (σ -T)~~ state caused by
18 ~~seismic slip and frictional melting~~slip along the nearby fault ~~surface~~. The ~~plagioclase feldspar~~ aggregates retain
19 the crystallographic orientation of ~~the host rock their host~~ and ~~shape preferred orientation relative are~~ elongated
20 ~~subparallel~~ to the ~~fault slip surface~~pseudotachylyte. We propose that plagioclase partially amorphized along the
21 microfractures at peak stress conditions followed by repolymerization to form dislocation-free grain aggregates
22 ~~within the timeframe of pseudotachylyte formation~~. ~~Repolymerization and recrystallization were enhanced by The~~
23 ~~heat from the slip surface dissipated into the wall rock causing a short lived temperature peak~~~~the infiltration of~~
24 ~~fluids that transported Ca and K into the microfractures~~. Subsequent cooling led to exsolution of intermediate
25 plagioclase compositions ~~by spinodal decomposition within a few millimeters distance to the fault surface~~~~and the~~
26 ~~formation of the Bøggild-Hunterlocher intergrowth in the grains from the fracture closest to the pseudotachylyte~~.
27 Our findings ~~provide microstructural evidence for the high σ -T conditions that are expected in the proximity of~~
28 ~~seismic faults, highlighting the importance of micro- and nanostructures for the understanding of earthquakes~~
29 ~~ruptures, and provide unequivocal evidence that fluid introduction~~the introduction of fluids in the microfractures
30 ~~occurred within the timescale of the thermal perturbation, prompting rapid annealing of damaged wall rock soon~~
31 ~~after earthquake rupture.~~

32 1 Introduction

33 During continent-continent collisions, plagioclase-rich granulite- and amphibolite-facies rocks are strong, dry and
34 prone to seismic faulting. ~~This is observed in some settings to allow fluid infiltration and subsequent~~
35 ~~metamorphism of the dry crust and subsequent metamorphism~~ (Jamtveit et al., 2016). Plagioclase responds ~~to~~
36 ~~lower crustal earthquakes~~ by microfracturing and fragmentation followed by fluid- and stress-induced
37 recrystallization (Mukai et al., 2014; Petley-Ragan et al., 2018; Soda and Okudaira, 2018). Grain size reduction

38 by fracturing and subsequent [nucleation and recrystallization](#) ~~and nucleation~~ localizes strain in the lower crust,
39 defining a transition from brittle to crystal-plastic deformation mechanisms with the potential to develop into shear
40 zones (Svahnberg and Piazzolo, 2010; Menegon et al., 2013; Okudaira et al., 2016; Marti et al., 2017). Thus,
41 recrystallization and subsequent shear may overprint any microstructural record of the high-intensity stress
42 conditions created by an earthquake. Analysis of plagioclase microstructures that have not undergone extensive
43 ~~annealing~~ [recrystallization](#) [MOU2] may provide valuable insight into the ~~stress and temperature~~ [mechanical and](#)
44 [thermal stress state](#) experienced by the wall rock during a seismic event.

45 In a purely elastic model, Reches and Dewers (2005) showed that for a dynamic earthquake rupture propagating
46 at 91% of the Rayleigh wave speed wall rock stresses may approach 10 GPa within 3 mm of a propagating rupture.
47 Furthermore, for ambient lower crustal temperatures in the range 600-700°C, the transient temperature following
48 an earthquake may exceed 1000°C within 1 cm of the slip surface (Bestmann et al., 2012; Clerc et al., 2018). Such
49 conditions, although short-lived, are expected to drive irreversible processes within the rock record. Extensive wall
50 rock fragmentation without shear strain around amphibolite and eclogite facies faults provide some evidence for
51 the high stresses caused by the propagation of seismic ruptures (Austrheim et al., 2017; Petley-Ragan et al., 2019).
52 Recent experimental studies have reported generation of amorphous material associated with fracturing and
53 seismic slip under eclogite facies conditions (Incel et al., 2019). On the other hand, thermal radiation around
54 frictional melt veins can drive recrystallization processes and form fine-grained dislocation-free aggregates
55 (Bestmann et al., 2012; 2016). Signatures such as these are beneficial in ~~extracting rupture and melting~~
56 ~~properties~~ [recording the short-lived mechanical and thermal anomalies](#) ~~of~~ [around](#) seismic faults.

57 Here we present a microstructural study of co-seismic microfractures in plagioclase from granulites in the [Lindås](#)
58 [Nappe of the Bergen Arcs](#) ~~of~~ [in](#) Western Norway at varying distances to a lower crustal pseudotachylyte (Fig. 1a).
59 [Our study builds directly on work done by Petley-Ragan et al. \(2018\) who analyzed the same microfractures in](#)
60 [plagioclase with electron backscatter diffraction \(EBSD\). They concluded that the microfractures formed as a](#)
61 [result of co-seismic damage in the wall rock adjacent to an earthquake fault and hypothesized that the grains](#)
62 [recrystallized within the timescale of pseudotachylyte crystallization.](#) ~~Microfractures previously described by~~
63 ~~Petley-Ragan et al. (2018) were analyzed with~~ [We use](#) a transmission electron microscope (TEM) equipped with
64 an energy dispersive X-ray (EDX) detector to observe the fine-grained aggregates at the nanoscale. Our combined
65 microstructural and chemical study aims at unravelling the thermo-mechanical evolution of plagioclase during and
66 after earthquake rupture.

67 **2 Geological Setting**

68 The Lindås Nappe of the Bergen Arcs of Western Norway is host to a population of seismic faults identified by
69 the presence of mm- to ~~em~~ [cm](#)-thick pseudotachylytes that cut through granulite facies anorthosite (Austrheim and
70 Boundy, 1994). The pseudotachylytes contain either an eclogite-facies or amphibolite-facies mineralogy, and the
71 wall rock damage adjacent to them are spatially related to fine-grained products of the same metamorphic grade.
72 The earthquakes took place within the lower crust during the Caledonian collision at 423-429 Ma (Jamtveit et al.,
73 2019) and provoked fluid-driven amphibolitization at 600°C and 0.8-1.0 GPa (Jamtveit et al., 2018), and
74 eclogitization at 650-750°C and 1.5-2.2 GPa (Jamtveit et al., 1990; Boundy et al., 1992; Glodny et al., 2008;
75 Bhowany et al., 2017). The wall rock damage is best observed on the micro-scale due to the high [spatial](#) density

76 of microfractures (<50 μm thick) that criss-cross the wall rock mineral phases (Fig. ~~1b and e~~ [MOU3]).
77 Microfractures in the most abundant mineral constituent of the granulite, plagioclase feldspar, were studied in
78 detail by Petley-Ragan et al. (2018) and are further investigated here on the nano-scale.

79 4.3 Methods

80 Photomicrographs of the plagioclase microstructures were taken with a Hitachi SU5000 field emission electron
81 microscope (FE-SEM) at the University of Oslo's Department of Geoscience. Chemical maps of the plagioclase
82 were obtained with a Cameca SX100 electron microprobe analyzer (EMPA) at the University of Oslo's
83 Department of Geoscience. The working conditions for EMPA were a beam diameter of 1 μm , an accelerating
84 voltage of 15 kV and a beam current of 10 nA. The EMPA maps were used to perform mass balance calculations
85 of three plagioclase microfractures. After segmenting the feldspar in the microfracture ~~area~~ from their host ~~area~~,
86 the average composition of the ~~microfracture~~ feldspar grains was compared to the average composition of the
87 surrounding plagioclase host. All other phases were excluded in the mass balance calculation.

88 3.1 Electron backscatter diffraction

89 Electron backscatter diffraction (EBSD) of the microfractures was done with a CamScan X500FE Crystal Probe
90 equipped with an Oxford/Nordlys detector at Geosciences Montpellier at the University of Montpellier in France.
91 The EBSD detector was run with an accelerating voltage of 17 kV and a step size of 0.2 μm at a sample tilt of 70°
92 and a working distance of 25 mm. The toolbox MTEX (version 4.4.0) in Matlab was used to obtain phase maps,
93 pole figures and grain parameters from the EBSD data (Bachmann et al., 2010; Hielscher and Schaeben, 2008). In
94 the phase maps, high-angle boundaries in black are defined by misorientations $\geq 10^\circ$ -while low-angle boundaries
95 in grey are defined by misorientations $< 10^\circ$. Further details on the analysis of the EBSD data along with links to
96 the raw data can be found in Petley-Ragan et al. (2018).

97 The grain sizes were extracted from the EBSD data to fit a probability density function (pdf) to their size
98 distribution. The fitting method is the same that is presented in Aupart et al. (2018). The pdf returns the probability
99 of encountering a grain of a given size using the Freedman-Diaconis rule to estimate the optimal number of bins
100 for a given grain size population. The number of bins were restricted to 15-25. Grain size distributions have been
101 fitted using two different power laws representative of small and large grains. The small grain size slope is referred
102 to as α_1 and large grain size slope is referred to as α_2 .

103 3.2 Transmission electron microscopy

104 ~~Mass balance calculations were performed on three microfractures by comparing the bulk microfracture~~
105 ~~composition to the bulk host composition. Electron microprobe maps of the microfractures were obtained with a~~
106 ~~Cameca SX100 at the University of Oslo's Department of Geosciences. The mass balance was calculated in~~
107 ~~MATLAB. Focused ion beam (FIB) foils were prepared and TEM analyses were carried out at the Department of~~
108 ~~Earth Sciences at Utrecht University. The FEI Helios Nanolab G3 was used to cut FIB foils perpendicular to the~~
109 ~~length of the microfractures and ~15-20 μm in length in order to include both the host and microfracture~~
110 ~~constituents (Fig. 1d and e). The FEI Talos 200FX equipped with a high-sensitive 2D energy dispersive X-ray~~
111 ~~(EDX) system was used to obtain bright-field (BF), dark-field (DF) and high angular annual dark-field (HAADF)~~

112 images in scanning TEM (STEM) mode. Large area EDX maps were acquired of the entire FIB foil for MF1 and
113 parts of the FIB foil for MF2.

115 3.3 Thermal diffusion model

116 In order to constrain the temperature history of each microfracture as a result of the nearby pseudotachylyte, we
117 modelled the diffusion of heat from the pseudotachylyte into the wall rock. The diffusion of heat into the wall rock
118 was calculated using a 1D steady-state thermal diffusion model from Bestmann et al. (2012). The model used an
119 ambient eclogite facies temperature (T_b) of 700°C for the wall rock (Jamtveit et al., 1990) and a melting
120 temperature (T_m) for granulite of 1500°C (Clerc et al., 2018). The model was calculated over a timescale (t) of
121 1000 seconds from initial frictional heating along the fault. With these parameters, the temperature (T) in Kelvin
122 at a certain distance (x) from the center of the pseudotachylyte can be expressed as,

$$123 \quad T(x, t) = 1/2(T_m - T_b) \{ \text{erf}[(1 - x/a)/2(\kappa t)^{1/2}] + \text{erf}[(1 + x/a)/2(\kappa t)^{1/2}] \}$$

124 At distances less than the half thickness of the pseudotachylyte (x), a thermal diffusivity (κ) of 0.72 mm²/s was
125 used for the molten pseudotachylyte (Di Toro and Pennacchioni, 2004) while at distances greater than the half
126 thickness, a thermal diffusivity (κ) of 0.48 mm²/s was used to represent the granulite wall rock (Clerc et al., 2018).
127 The temperature evolution at the distance representing each microfracture was studied.

128 3-4 Results Plagioclase wall rock damage

129 Two microfractures of dominantly plagioclase and K-feldspar previously described by Petley-Ragan et al. (2018)
130 were subject to further study with transmission electron microscopy (TEM). Both microfractures are located
131 adjacent to a 1.3 mm thick eclogite facies pseudotachylyte. The microfracture orientations are independent of the
132 crystallographic orientation of the host grains. The microfractures contain fine-grained aggregates (grain size <5
133 µm) of dominantly plagioclase and K-feldspar (Fig. 2a and b). The microfracture from Figures 1b and d will
134 hereafter be referred to as Microfracture 1 (MF1) and is located 1.25 mm away from pseudotachylyte with a mean
135 grain size of 1.73 µm² (Aupart et al., 2018). The microfracture from Figure 1c and e will be referred to as
136 Microfracture 2 (MF2) and is located 1.8 cm away from the same pseudotachylyte (Fig. 1a) with a mean grain size
137 of 2.14 µm² (Aupart et al., 2018). MF2 also contains a set of secondary fractures (Fig. 1c). The presence of
138 secondary fractures indicates that MF2 experienced more shear deformation than MF1 (Petley-Ragan et al., 2018).

139 4.1 Structure and composition of the microfractures

140 ~~Microfractures in wall rock plagioclase are found across the island of Holsnøy, adjacent to both types of~~
141 ~~pseudotachylytes, and their orientations are independent of the crystallographic orientation of the host grains. The~~
142 ~~microfractures contain fine-grained aggregates (grain size <5 µm) of dominantly plagioclase and K-feldspar (Fig.~~
143 ~~1d and e). The grains within the microfractures have a crystallographic preferred orientation (CPO) that is~~
144 ~~controlled by the host plagioclase on either side of the microfracture (Fig. 2 c and d) (Fig. 2), and the K-feldspar~~
145 ~~grains have a CPO that mimics that of the plagioclase grains (Petley-Ragan et al., 2018; Petley-Ragan et al., 2018).~~
146 ~~The grains also show a strong shape preferred orientation (SPO) with the long axis parallel to the pseudotachylyte~~

147 wall irrespective of the microfracture orientation (Fig. 2e and f). Plagioclase compositions in the ranges An₂₅₋₃₁
148 and An₆₅₋₈₃ were measured in the microfractures. These originate from a host composition of An₄₀ (Petley-Ragan
149 et al., 2018). A similar bimodal range of plagioclase compositions were ~~also~~ observed at garnet-plagioclase phase
150 boundaries and in an amphibolite facies micro-shear zone at Isdal ca. 40 km NE of Holsnøy (Mukai et al., 2014).
151 Mass balance calculations based on three microfractures show that there is 5-11 times more K in the microfractures
152 compared to the host composition (Fig. 3). Additionally, the microfractures are enriched in Ca and depleted in Na
153 compared to their host.

154 ~~The mineralogy of the microfractures and their associated reaction products varies locally. Some contain quartz~~
155 ~~and kyanite, while others are associated with intergrowths of clinozoisite, quartz and K-feldspar. The~~
156 microfractures locally consist of quartz and kyanite, or intergrown clinozoisite, quartz and K-feldspar. A few
157 microfractures contain minor amounts of carbonates or phengite. ~~Microfracture mineralogy is found to depend on~~
158 ~~the X_{CO₂} of the infiltrating fluid (Okudaira et al., 2016) and the orientation of the microfracture relative to the~~
159 ~~principle stress (Moore et al., 2019). The detailed evolution of the microfractures is thus dependent on a multitude~~
160 ~~of factors. [MOU4]~~

161 The distribution of plagioclase grain sizes from each microfracture are displayed in Figure 4. Both distributions
162 show power law slopes with a crossover from a shallow slope (-1.1 and -1.4) for small grain sizes to a steeper
163 slope (-2.7 and -3.4) for large grain sizes. The crossover occurs near the mean value of the grain size and the steep
164 slopes for the larger grains is reflected by the essentially equigranular appearance of this microstructure.

165 4.2 TEM Results

166 ~~Two microfractures of dominantly plagioclase and K-feldspar previously described by Petley-Ragan et al. (2018)~~
167 ~~were subject to further study with transmission electron microscopy (TEM). The grain size distributions within~~
168 ~~these microfractures were characterized by electron backscatter diffraction (EBSD) (Aupart et al., 2018). The~~
169 ~~microfracture from Figure 1d will hereafter be referred to as Microfracture 1 (MF1) and is located 1.25 mm away~~
170 ~~from pseudotachylyte with a mean grain size of 1.73 μm^2 (Aupart et al., 2018). The microfracture from Figure 1d~~
171 ~~will be referred to as Microfracture 2 (MF2) and is located 1.8 cm away from the same pseudotachylyte (Fig. 1a)~~
172 ~~with a mean grain size of 2.14 μm^2 (Aupart et al., 2018). MF2 also contains a set of secondary fractures (Fig. 1c).~~
173 ~~Both microfractures are associated with clinozoisite, quartz and kyanite growth, and only MF2 contains dolomite.~~
174 ~~[MOU5] The lower J-index, greater misorientations and the presence of secondary fractures indicate that MF2~~
175 ~~experienced more shear deformation than MF1 (Petley-Ragan et al., 2018).~~

176 ~~4 Methods [MOU6]~~

177 ~~Mass balance calculations were performed on three microfractures by comparing the bulk microfracture~~
178 ~~composition to the bulk host composition. Electron microprobe maps of the microfractures were obtained with a~~
179 ~~Cameca SX100 at the University of Oslo's Department of Geosciences. The mass balance was calculated in~~
180 ~~MATLAB. Focused ion beam (FIB) foils were prepared and TEM analyses were carried out at Utrecht University.~~
181 ~~The FEI Helios Nanolab G3 was used to cut FIB foils perpendicular to the length of the microfractures and 15~~
182 ~~20 μm in length in order to include both the host and microfracture constituents (Fig. 1d and e). The FEI Talos~~
183 ~~200FX equipped with a high sensitive 2D energy dispersive X-ray (EDX) system was used to obtain bright field~~

(BF), dark field (DF) and high angular annular dark field (HAADF) images in scanning TEM (STEM) mode. Large area EDX maps were acquired of the entire FIB foil for MF1 and parts of the FIB foil for MF2.

5 Results

Mass balance calculations based on three microfractures show that there is 5–11 times more K in the microfractures compared to the host composition (Fig. 3). A bright field TEM image shows that MF1 contains dislocation-poor and dislocation-free grains of dominantly plagioclase and K-feldspar defined by straight grain boundaries with 120° triple junctions (Fig. 54a). Few grains contain single dislocation walls dislocations within their centre. In contrast, the host plagioclase is littered with contains a high density of free-dislocations that have formed a locally arranged to form a subgrain wall made up of closely spaced dislocations. Ankerite ($\text{Ca}(\text{Fe},\text{Mg})(\text{CO}_3)_2$), grossular-rich garnet and sphene are additional phases in MF1, with apatite and rutile inclusions inside the grains, pinned along grain boundaries and concentrated along the subgrain wall in the host (Fig. 54b).

The EDX map of MF1 displays homogeneous K-feldspar grains with homogeneous composition and plagioclase grains that are heterogeneous with respect to their CaAl and NaSi content (Fig. 54b). The K-feldspar grains are clustered together creating a fabric dominated by grain boundaries instead of phase boundaries. The irregular composition distribution of Na and Ca in the plagioclase grains contradicts the backscatter electron image that suggests Ca zoning around the grains (Fig. 1d and 54b). Instead, the Ca-rich domains locally overlie areas with submicron lamellae (Fig. 65a-f). The lamellae are discontinuous throughout the plagioclase grains and, locally, they are superimposed by tapered mechanical twins (Fig. 65a). Other grains contain both lamellae and twins that are spatially distinct but are parallel to each other (Fig. 65d). In some grains, the lamellae appear slightly curved (Fig. 65c) while in others, the lamellae appear to form a ‘tweed’ structure (Fig. 65f). The spacing between lamellae is approximately 10–30 nm. Due to the high The anorthite-rich domains -have a composition (An_{65-83} ; Petley-Ragan et al., 2018) obtained for plagioclase within this microfracture (An_{65-83} ; Petley-Ragan et al., 2018) this structure lies within the Bøggild-Huttenlocher miscibility gap (Smith and Brown, 1988; McConnell, 2008). The Bøggild-Huttenlocher intergrowth is Similar intergrowths are not observed within the host plagioclase.

MF2 is similarly dominated by dislocation-poor grains of plagioclase and K-feldspar with a number of grains displaying twinning (Fig. 76a). The twins of separate grains are approximately parallel to each other and to (010) of the host plagioclase (see Fig. 6 of Petley-Ragan et al., 2018), reinforcing the preservation of crystallographic orientations of the host through the fracturing and recovery process. Kyanite and a K-rich micaceous phase are additional phases in MF2. Apatite inclusions are present within the grains and pinned along grain boundaries. The fabric is defined-characterized by 120° triple junctions with rare dislocation-rich grains that display irregular boundaries (Fig. 76b).

The EDX map of MF2 shows clustered homogeneous K-feldspar grains and zoned plagioclase grains (Fig. 76c) creating again a grain boundary-dominated fabric. Unlike MF1, the plagioclase grains in MF2 display Ca-enrichment at their grain boundaries and the submicron lamellae are absent. The Ca-rich rims are approximately 100–200 nm thick.

4.3 Thermal Model Results

220 The temperature evolutions of MF1 and MF2 over 1000 seconds after frictional heating along the pseudotachylyte
221 are displayed in Figure 8. According to our steady-state thermal diffusion model, the temperature evolutions of
222 the microfractures are substantially different from one another. MF1 experienced a drastic increase in temperature
223 by up to ~135°C above ambient (reaching ~835°C) within a matter of seconds. By 100 seconds after heating, MF1
224 had cooled back to 740°C before gradual cooling to ambient temperature over the next few minutes. In contrast,
225 MF2 located about ~~two centimeters~~ 2 cm further away from the slip surface than MF1, experienced a gradual
226 increase to a peak temperature of ~15°C above ambient after 300 seconds. By 1000 seconds after frictional slip
227 along the fault, both microfractures had reached similar temperatures near ambient.

229 6.5 Discussion

230 The micro- and nano-scale structures of the microfractures described above offer insight into characterize the
231 evolution of wall rock plagioclase feldspar that resulted from the high-stress and high-temperature environment
232 perturbations created near an a lower crustal earthquake slip plane. The dislocation-free nature of almost all grains
233 in domains MF1 and MF2 suggest nearly complete annealing of the material within the microfractures (Fig. 54a
234 and 76a). The grain fabric is dominated by straight phase and grain boundaries, 120° triple junctions and pinned
235 apatite inclusions suggesting the migration of extensive grain boundary migrationies. The inheritance of the
236 crystallographic orientation of the host plagioclase and its twins within the grains, furthermore, points towards an
237 initial annealing process that is able to transfer and preserve crystallographic information (Fig. 3). An equilibrium
238 fabric with crystallographic inheritance is generally created by dislocation creep and grain boundary migration
239 (Passchier and Trouw, 2005). However, the parallel A pronounced shape preferred orientation (SPO) of the
240 grains parallel to the pseudotachylyte wall (Fig. 2) suggests that annealing was initiated while a stress or thermal
241 field generated by the with a consistent geometry orientation relative to the seismic slip plane was still present
242 (Petley-Ragan et al., 2018). If these fields were generated by an earthquake, This it would constrains the time scale
243 of initial microfracture annealing to the duration of pseudotachylyte crystallization and cooling (seconds to
244 minutes).

245 The observation of lamellae structures interpreted to have formed by unmixing of a Ca-rich plagioclase in the M1
246 sample, but not in the M2 sample, in MF1 but not MF2 is consistent with the M1 sample being formed at higher
247 temperatures and hence suggests that unmixing of grain growth plagioclase grains of intermediate compositions
248 occurred within the timescale of the local thermal anomaly. The Bøggild-Huntlocher miscibility gap takes place
249 below 800°C (Carpenter, 1994; McConnell, 2008), approximately 20 seconds after heating in MF1 (Fig. 8).
250 However, As, grain growth and recovery of chemical diffusion in silicates is known to be extremely slow under dry
251 conditions (Pennacchioni et al., 2020; Dunkel et al., 2021), this and would clearly require the presence of fluids.
252 Fluid introduction is also reflected by the presence of minor hydrous phases, such as clinozoisite and phengite,
253 and carbonates within these microfractures, as well as a significant increase in K compared to the host wall rock
254 plagioclase (Fig. 3). Furthermore, our mass balance illustrates an increase in Ca in the plagioclase aggregates
255 compared to their host which creates a composition that promotes unmixing below 800°C. Our observations thus
256 provide unequivocal evidence that dynamic rupturing and subsequent seismic slip was followed by fluid
257 infiltration on the time scale of within seconds-, altering the microfracture composition prior to recovery to minutes.

258 ~~If grain recovery and development of the pronounced SPO would have~~ occurred over much longer time-scales,
259 MF1 and MF2 ~~fractures w~~ould have ~~experienced~~ reached similar temperature conditions (Fig. 8) and the SPO
260 ~~must~~ would have been controlled by ~~some~~ a far-field stress. Assuming that the long axes of the plagioclase grains
261 are oriented ~~perpendicular~~ to the largest stress axis (σ_1), the observed SPO would ~~then~~ imply that the far-field σ_1
262 was perpendicular to the slip surface. This is inconsistent with the fault being developed as a shear fracture driven
263 by the same far-field ~~tectonic~~ stress that would have controlled the SPO. ~~Hence~~ Therefore, we propose that the
264 observed SPO ~~, as well as the unmixing observed in the M1 plagioclase~~ is more readily explained by a fast recovery
265 process and a local stress field that is controlled by the geometry of the pseudotachylyte. This is consistent with
266 studies by Bestmann et al. (2012, 2016) who suggest that dynamic recrystallization of damaged quartz occurred
267 within the short-lived thermal anomaly related to a seismic event.

268 The power-law grain size distributions of the MF1 and MF2 grain populations (Figure. 4), also support relatively
269 rapid recovery as a slow steady state growth process is expected to lead to a log-normal distribution of grain sizes
270 (Aupart et al., 2018). The extremely steep slopes characterizing the larger grain size fraction of the plagioclase
271 aggregates in the MF1 and MF2 microfractures are similar to what has previously been described from pulverized
272 garnet and olivine from the wall rocks of lower crustal seismic faults (Aupart et al., 2018). The origin of this
273 scaling is, however, not fully understood.

274 ~~Dislocation and grain boundary migration are too slow to have taken place within this time scale (MOU9), and it is~~
275 ~~additionally puzzling as to why these mechanisms were not active within the dislocation rich host. Thus, we~~
276 ~~postulate that a much more rapid recrystallization process (MOU10) took place prior to grain boundary migration and~~
277 ~~final annealing within the microfractures, and this process must have been focused and enhanced by local factors~~
278 ~~such as fluid infiltration and heat from the nearby pseudotachylyte. The resulting grain size distributions as~~
279 ~~discussed by Aupart et al. (2018) furthermore show striking deviations from a steady state distribution. (MOU11)~~

281 **6.15.1 Stressed wall rock Pre-recovery state of plagioclase**

282 Deformation experiments performed at eclogite facies conditions may offer some insight into the state of the
283 microstructures ~~that were present in~~ within the microfractures ~~before prior to complete~~ recovery. Incel et al. (2017;
284 2019) observed brittle fractures filled with amorphous material during deformation experiments on blueschist
285 under eclogite facies conditions. They interpreted the amorphous material to result from shock loading during the
286 propagation of a dynamic rupture. Although their experiments involved a short recovery time (<1 hour) some of
287 the amorphous material recrystallized, creating idiomorphic garnet crystals with a size of ~20 nm.

288 ~~A~~ The amorphization of plagioclase feldspar is dependent on pressure (P), temperature (T), composition (X),
289 compression rate (P/t) and pressure duration (t). Amorphization that is strongly dependent on temperature is
290 commonly referred to as heterogeneous amorphization or melting, and is a relatively slow process due to its
291 dependence on the diffusion of atoms (Wolf et al., 1990). On the other hand, amorphization that is strongly
292 dependent on pressure, ~~is referred to as~~ pressure-induced amorphization, ~~which~~ may be static or dynamic,
293 depending on the compression rate (Sharma and Sikka, 1996). ~~For In~~ the following, ~~the we will discuss~~ pressure-
294 induced amorphization ~~of plagioclase will be discussed~~. For anorthite-rich compositions (An₅₁₋₁₀₀) complete

295 pressure-induced amorphization occurs [at pressures \$P \geq 13\$ GPa](#) and $T = 660^\circ\text{C}$, while albite-rich (An_2)
296 compositions are not completely amorphous until $P \geq 26$ GPa and $T = 950^\circ\text{C}$ (Daniel et al., 1997; Kubo et al.,
297 2009; Tomioka et al., 2010). [Furthermore, a short pressure durations results](#) in lower degrees of amorphization
298 (Tomioka et al., 2010) while high compression rates of 10^1 - 10^2 GPa/s can reduce the pressure required for
299 amorphization (Sims et al., 2019). The short-lived (microseconds) high intensity (10^6 GPa/s) conditions in the
300 proximity of earthquake rupture tips (Reches and Dewers, 2005) may partially amorphize plagioclase feldspar
301 (An_{40}) in the wall rock, even if the local pressure for *complete* amorphization is not reached. The presence of
302 asymmetric tensile cracks on some of the microfractures indicates that the propagation velocity of the
303 microfractures approached the shear wave velocity (Petley-Ragan et al., 2018) inducing similar short-lived high-
304 intensity stresses within their vicinity. Therefore, a mixture of amorphous material with remnant fragments may
305 have been present within the microfractures immediately after earthquake and microfracture rupture.

306 Repolymerization of amorphous material on the microfracture walls and remnant fragments would directly transfer
307 the crystallographic orientation of the host. Crystallographic information may also be preserved by the presence
308 of short-range atomic order within amorphous material, allowing for immediate repolymerization without the aid
309 of a fragment nucleus (Casey et al., 1993; Konrad-Schmolke et al., 2018). Repolymerization has also been
310 suggested to occur directly along crystal lattice defects where amorphous material originates (Konrad-Schmolke
311 et al., 2018). In this context, dislocations within the grains may have healed much more quickly than would be
312 expected from dislocation migration recrystallization and the fragments would have experienced healing from
313 multiple available interfaces. Other preferred areas of repolymerization were likely parallel to the minimum
314 principal stress direction, growing grains with a stress-dependent SPO. Therefore, recrystallization from an
315 amorphous material may be a likely candidate to create the observed dislocation-free fabric with a strong SPO
316 within [the timeframe of pseudotachylyte formation seconds to minutes after seismic slip](#).

317 **6.2 Cooling within the vicinity of pseudotachylyte**

318 [The nano scale intergrowth within the plagioclase grains from MFI is here interpreted as exsolution lamellae that](#)
319 [formed as a result of rapid cooling from high temperatures within the vicinity of the pseudotachylyte. Similar](#)
320 [intergrowths were found in what is called the 'complex feldspar', a microstructure of fragmented plagioclase first](#)
321 [described in an amphibolite facies shear zone at Isdal, approximately 40 km east of Holsnøy \(Mukai et al., 2014\).](#)
322 [They interpreted the structure as fluid- and stress-induced coarsening of exsolution lamellae. Although plausible,](#)
323 [this would require that plagioclase exsolution occurred prior to the stress and thermal anomaly created by the](#)
324 [earthquake. No intergrowths are observed within the host plagioclase in the present study, and it is unlikely that](#)
325 [diffusion rates were high enough to form lamellae within the dry granulite. Our documentation of the exsolution](#)
326 [lamellae within plagioclase grains from the microfracture nearest the pseudotachylyte \(Fig. 1a\) suggests that the](#)
327 [thermal anomaly produced by the frictional melt vein affected the intracrystalline structure of the plagioclase grains.](#)

328 [Intergrowths form when plagioclases of intermediate composition cool from high temperature and enter a](#)
329 [miscibility gap below \$800^\circ\text{C}\$, exsolving into separate calcic and sodic regions \(Carpenter, 1994; McConnell, 2008\).](#)
330 [Although the ambient eclogite facies conditions \(\$650\$ - \$750^\circ\text{C}\$ \) place the plagioclase within the miscibility gap, the](#)
331 [absence of fluids hinders chemical diffusion and thus exsolution. It is only until after an earthquake causes wall](#)
332 [rock damage that fluids enter the wall rock through coseismic microfractures, and these fluids are likely overheated](#)

333 by the frictional slip (Bestmann et al., 2016). Simultaneously, the wall rock within <1 cm of the pseudotachylyte
334 experiences a thermal anomaly before rapidly cooling back to ambient conditions at rates on the order of a few °C/s
335 (Bestmann et al., 2012). NaSi-CaAl diffusivity in plagioclase at 900–1000°C is $\sim 10^{-15}$ cm²/s (Korolyuk and Lepezin,
336 2009). Assuming that elevated temperatures lasted for up to a minute within 1 mm of the pseudotachylyte (MF1),
337 diffusion would be efficient over a distance of 25 nm, similar to the spacing of lamellae observed (Fig. 5). At
338 distances greater than 1 cm from the pseudotachylyte (MF2), the wall rock experiences minor heating to a few
339 10°C above ambient. Therefore, rapid cooling from elevated temperatures back to ambient conditions and into the
340 miscibility gap only took place within close proximity to the pseudotachylyte. **5.2 The role of fluids** Microfracture
341 mineralogy is found to depend on the X_{CO_2} of the infiltrating fluid (Okudaira et al., 2016) and the orientation of
342 the microfracture relative to the principle stress (Moore et al., 2019). The detailed evolution of the microfractures
343 is thus dependent on a multitude of factors.

344 Recent studies of seismic faults in lower crustal granulites have demonstrated that under dry conditions, both mass
345 transfer and microstructural recovery is very limited. Even relict amorphous material has been reported from within
346 the pseudotachylyte itself (Pennacchioni et al., 2020; Dunkel et al., 2021). The microstructures and mineralogical
347 effects observed in the wall rock microfractures in ~~the present~~ our study, including the presence of minor hydrous
348 phases and carbonates, clearly reflect the introduction of fluids at a very early stage ~~of~~ after earthquake
349 development. The maximum rate of fluid migration in the wake of a dynamic rupture connected to a fluid reservoir
350 is still poorly constrained. However, ~~yet~~ unpublished modelling results by our group ~~in Oslo~~ at the University of
351 Oslo indicate that incipient water migration rates in tensile microcracks may reach a significant fraction of the
352 Rayleigh velocity.

353 The consumption of fluids by fluid-consuming reactions in the wall rocks would maintain fluid pressure gradients
354 that would drive sustained fluid migration into the wall rocks as demonstrated by Malvoisin et al. (2020). These
355 authors presented petrological data and numerical models indicating that in the presence of fluids, densification
356 associated with eclogite-forming reactions ~~reactions~~ would occur within weeks, and consume fluids injected
357 during and immediately after an earthquake.

358 The source of fluids during eclogitization in the Bergen Arcs has been discussed for several decades. Svensen et
359 al. (~~2001~~1999) demonstrated that aqueous brines entering a dry granulite under eclogite facies conditions may get
360 extremely enriched in a variety of solutes during hydration reactions and thus represent an effective medium for
361 substantial mass transfer ~~even~~ in a relatively fluid-poor system. This may explain the chemical difference between
362 the original wall rock plagioclase and the feldspar aggregates observed in the microfractures (Fig. 3).- Recently,
363 Jamtveit et al. (2021-submitted) show that shear heating of Lower Paleozoic metapelites located in the immediate
364 footwall of the Lindås Nappe ~~may have resulted in dehydration and fluid production~~ may have dehydrated and
365 contributed to fluid production during Nappe emplacement. To what extent this fluid production has contributed
366 to the brittle failure of the overlying lower crust is still not well constrained.

368 **7-6 Conclusion**

369 Our nanostructural observations are relevant for understanding plagioclase deformation during and after an
370 earthquake in the lower crust, prior to any subsequent shear zone development. We propose that plagioclase within
371 the microfractures experienced partial amorphization at peak pressures coeval with earthquake propagation and
372 microfracturing in the wall rock. Repolymerization on microfracture walls, remnant fragments, ~~dislocations~~ and
373 from short-range atomic ordering in the direction parallel to the minimum principal stress formed a strong CPO
374 and SPO in the grains. Repolymerization and ~~recrystallization~~ recovery within the timeframe of pseudotachylyte
375 formation explains the presence of dislocation-free grains, as has been interpreted for similar structures observed
376 in quartz (Bestmann et al., 2012, 2016). In close proximity to the pseudotachylyte, wall rock temperatures reached
377 ~~~900-1000~~ 850°C before rapidly cooling back to ambient eclogite facies conditions and into the plagioclase
378 miscibility gap. This caused exsolution of intermediate plagioclase compositions and the formation of nano-scale
379 lamellae. Yet, the complete recrystallization of the material in the microfractures and the exsolution of plagioclase
380 to form lamellae would not have been possible without the presence of fluids. We hypothesize that the lamellae
381 described here are a unique signature of ~~rapid-cooling~~ fluid-driven recrystallization within plagioclase-rich wall
382 rock in the vicinity of pseudotachylyte. ~~A study of a larger number of plagioclase microfractures at varying~~
383 ~~distances to pristine pseudotachylyte would provide more information and constraints on the occurrence of these~~
384 ~~intergrowths.~~ ~~The dependence of plagioclase microstructures on temperature and cooling rate and their sensitivity~~
385 ~~to fluid interaction offers a new tool for unraveling the history of wall rocks and their associated~~
386 ~~earthquakes.~~ observed microstructures and associated mass transfer demonstrate that externally derived fluids
387 entered the wall rock microfractures on the time scale of the earthquake.

388 **Data and Sample Availability**

389 Raw electron backscatter diffraction and geochemical data are available on Open Science Framework at
390 osf.io/g36m7/. Rock samples are available through A. P.-R. and FIB foils are available through O. P.

391 **Author Contribution**

392 B. J. designed the project. A. P.-R. collected the samples, obtained and analyzed the EBSD and geochemical data.
393 B. I. helped collect and interpret the EBSD data. O. P. cut the FIB foils, and obtained and interpreted the TEM
394 images. A.P.-R., O. P. and B. J. were part of discussions. A. P.-R. and B. J. wrote the manuscript.

395 **Competing Interests**

396 The authors declare that they have no conflict of interest.

397 **Acknowledgements**

398 This project was supported by the European Research Council (ERC) Advanced Grant Agreement 669972,
399 “Disequilibrium Metamorphism” (“DIME”) to B. J., and the Natural Science and Engineering Research Council
400 (NSERC) of Canada Postgraduate Scholarship Doctoral (PGS-D) 489392 to A. P.-R. O. P. has been supported by
401 an ERC Starting Grant “nanoEARTH” (852069). We thank H. Austrheim for field guidance on Holsnøy and
402 hospitality in Western Norway. We thank X. Zhong for help with the mass balance calculations, F. Barou for
403 assistance with EBSD measurements and M. Erambert for help on the electron microprobe. Lastly, we greatly
404 appreciate the thorough revisions by Mark Pearce and an anonymous reviewer that have improved the manuscript.

405 **References**

- 406 [Aupart, C., Dunkel, K. G., Angheluta, L., Austrheim, H., Ildefonse, B., Malthe-Sørenssen, A., and Jamtveit, B.:](#)
407 [\(2018\). Olivine grain size distributions in faults and shear zones: Evidence for nonsteady state](#)
408 [deformation. ~~Journal of Geophysical Research~~J. Geophys. Res.: Solid Earth, 123, 7421–7443.](#)
409 <https://doi.org/10.1029/2018JB015836>, 2018.
- 410 Austrheim, H. and Boundy, T. M.: Pseudotachylytes generated during seismic faulting and eclogitization of the
411 deep crust, *Science*, 265, 82-83, <http://www.jstor.org/stable/2884364>, 1994.
- 412 Austrheim, H., Dunkel, K. G., Plümper, O., Ildefonse, B., Liu, Y., and Jamtveit, B.: Fragmentation of wall rock
413 garnets during deep crustal earthquakes, *Sci. Adv.*, 3, 1-8, <https://doi.org/10.1126/sciadv.1602067>, 2017.
- 414 [Bachmann, F., Hielscher, R., & Schaeben, H.: \(2010\).–Texture analysis with MTEX – free and open source](#)
415 [software toolbox. *Solid State Phenom.*, 160, 63-68. doi:10.4028/www.scientific.net/SSP.160.63, 2010.](#)
- 416 Bestmann, M., Pennacchioni, G., Nielsen, S., Göken, M., and de Wall, H.: Deformation and ultrafine dynamic
417 recrystallization of quartz in pseudotachylyte-bearing brittle faults: A matter of a few seconds. *J. Struct.*
418 *Geol.*, 38, 21-38, <https://doi.org/10.1016/j.jsg.2011.10.001>, 2012.
- 419 Bestmann, M., Pennacchioni, G., Mostefaoui, S., Göken, M. and de Wall, H.: Instantaneous healing of micro-
420 fractures during coseismic slip: Evidence from microstructure and Ti in quartz geochemistry within an
421 exhumed pseudotachylyte-bearing fault in tonalite, *Lithos*, 254-255, 84-93,
422 <https://doi.org/10.1016/j.lithos.2016.03.011>, 2016.
- 423 Bhowany, K., Hand, M., Clark, C., Kelsey, D. E., Reddy, S. M., Pearce, M. A., Tucker, N. M., and Morrissey, L.
424 J.: Phase equilibria modelling constraints on P-T conditions during fluid catalysed conversion of granulite
425 to eclogite in the Bergen Arcs, Norway, *J. Metamorph. Geol.*, <https://doi.org/10.1111/jmg.12294>, 2017.
- 426 Boundy, T.M., Fountain, D.M., and Austrheim, H.: Structural development and petrofabrics of eclogite facies
427 shear zones, Bergen Arcs, western Norway: implications for deep crustal deformational processes, *J.*
428 *Metamorph. Geol.*, 10, 2, 127-146, <https://doi.org/10.1111/j.1525-1314.1992.tb00075.x>, 1992.
- 429 Carpenter, M. A.: Mechanisms and kinetics of Al-Si ordering in anorthite: I. Incommensurate structure and domain
430 coarsening, *Am. Mineral.*, 76, 1110-1119, 1991.
- 431 Casey, W. H., Westrich, H. R., Banfield, J. F., Ferruzzi, G. and Arnold, G. W.: Leaching and reconstruction at the
432 surfaces of dissolving chain-silicate minerals, *Nature*, 366, 253-256, <https://doi.org/10.1038/366253a0>,
433 1993.
- 434 [Clerc, A., Renard, F., Austrheim, H. and Jamtveit, B.: Spatial and size distributions of garnets grown in a](#)
435 [pseudotachylyte generated during a lower crustal earthquake. *Tectonophys.*, 733, 159-170.](#)
436 <https://doi.org/10.1016/j.tecto.2018.02.014>, 2018.
- 437 Daniel, I., Gillet, P., McMillan, P. F., Wolf, G. and Verhelst, M. A.: High-pressure behavior of anorthite:
438 Compression and amorphization. *J. Geophys. Res.*, 102, 10313-10325.
439 <https://doi.org/10.1029/97JB00398>, 1997.
- 440 [Di Toro, G. and Pennacchioni, G.: Superheated friction-induced melts in zoned pseudotachylytes within the](#)
441 [Adamello tonalites \(Italy, Southern Alps\). *J. Struct. Geol.*, 26, 10, 1783-1801,](#)
442 <https://doi.org/10.1016/j.jsg.2004.03.001>, 2004.

443 [Dunkel, K. G., Morales, L. F. G., and Jamtveit, B.: ,2021, Pristine microstructures in pseudotachylytes formed in](#)
444 [dry lower crust, Lofoten, Norway. *Philosophical Transactions A, Phil. Trans. R. Soc. A*, 379: 20190423,](#)
445 [, 2021.](https://doi.org/10.1098/rsta.2019.0423)

446 Glodny, J., Kühn, A., and Austrheim, H.: Geochronology of fluid-induced eclogite and amphibolite facies
447 metamorphic reactions in subduction-collision system, Bergen Arcs, Norway. *Contrib. Mineral. Petr.*,
448 156, 1, 27-48, <https://doi.org/10.1007/s00410-007-0272-y>, 2008.

449 ~~[Hielscher, R. and Schaeben, H.: \(2008\)–A novel pole figure inversion method: specification of the MTEX](#)~~
450 ~~[algorithm. *Journal of Applied Crystallography*. *J. Appl. Crystal.*, 41, —41, 1024-1037.:](#)~~
451 ~~[doi:10.1107/S0021889808030112](https://doi.org/10.1107/S0021889808030112), 2008.:~~

452 Incel, S., Hilairet, N., Labrousse, L., John, T., Deldicque, D., Farrand, T., Wang, Y., Renner, J., Morales, L. and
453 Schubnel, A.: Laboratory earthquakes triggered during eclogitization of lawsonite-bearing blueschist.
454 *Earth Planet. Sci. Lett.*, 459, 320-331, <https://doi.org/10.1130/G45527.1>, 2017.

455 [Incel, S., Schubnel, A., John, T., Freeman, H., Wang, Y., Renard, F., and Jamtveit, B.: Experimental evidence for](#)
456 [wall rock pulverization during dynamic rupture at ultra-high pressure conditions. *Earth Planet. Sci. Lett.*,](#)
457 [528, 115832, https://doi.org/10.1016/j.epsl.2019.115832](https://doi.org/10.1016/j.epsl.2019.115832), 2019.

458

459 ~~[Incel, S., Schubnel, A., John, T., Freeman, H., Wang, Y., Renard, F., Jamtveit, B., 2019, Experimental evidence](#)~~
460 ~~[for wall rock pulverization during dynamic rupture at ultra-high pressure conditions. *Earth and Planetary Science*](#)~~
461 ~~[Letters](#), 528, 115832~~

462 ~~[Incel, S., Labrousse, L., Hilairet, N., John, T., Gase, J., Shi, F., Wang, Y., Andersen, Renard, F., Jamtveit, B. And](#)~~
463 ~~[Schubnel, A.: Reaction induced embrittlement of the lower continental crust, *Geology*, 47, 3, 235-238,](#)~~
464 ~~<https://doi.org/10.1130/G45527.1>, 2019.~~

465 Jamtveit, B., Austrheim, H., and Putnis, A.: Disequilibrium metamorphism of stressed lithosphere, *Earth Sci. Rev.*,
466 154, 1-13. <https://doi.org/10.1016/j.earscirev.2015.12.002>, 2016.

467 Jamtveit, B., Bucher-Nurminen, K. and Austrheim, H.: Fluid controlled eclogitization of granulites in deep crustal
468 shear zones, Bergen Arcs, Western Norway, *Contrib. Mineral. Petr.*, 104, 184-193,
469 <https://doi.org/10.1007/BF00306442>, 1990.

470 Jamtveit, B., Moulas, E. Andersen, T. B., Austrheim, H., Corfu, F., Petley-Ragan, A. and Schmalholz, S. M.: High
471 pressure metamorphism caused by fluid induced weakening of deep continental crust. *Sci. Rep.*, 8, 17011,
472 <https://doi.org/10.1038/s41598-018-35200-1>, 2018.

473 Jamtveit, B., Petley-Ragan, A., Incel, S., Dunkel K. G., Aupart, C., Austrheim, H., Corfu, F., Menegon, L. and
474 Renard, F.: The effects of earthquakes and fluids on the metamorphism of the lower continental crust, *J.*
475 *Geophys. Res.*, 124, 8, 7725-7755, <https://doi.org/10.1029/2018JB016461>, 2019.

476 [Jamtveit, B., Dunkel, K., Petley-Ragan, A., Austrheim, H., Corfu, F., and Schmid, D. W.: Rapid fluid-driven](#)
477 [transformation of lower continental crust associated with thrust-induced shear heating, *Lithos*, submitted.](#)

478 Konrad-Schmolke, M., Halama, R., Wirth, R., Thomen, A., Klitscher, N., Morales, L., Schreiber, A. and Wilke,
479 F. D. H.: Mineral dissolution and reprecipitation mediated by an amorphous phase, *Nature contrib.*, 9,
480 <https://doi.org/10.1038/s41467-018-03944-z>, 2018.

481 Kubo, T., Kimura, M., Kato, T., Nishi, M., Tominaga, A., Kikegawa, T. and Funakoshi, K.: Plagioclase breakdown
482 as an indicator for shock conditions of meteorites, *Nat. Geosci.*, 3, 41-45, <https://doi.org/10.1038/ngeo704>,
483 2009.

484 Marti, S., Stünitz, H., Heilbronner, R., Plümper, O. and Drury, M.: Experimental investigation of the brittle-viscous
485 transition in mafic rocks – Interplay between fracturing, reaction, and viscous deformation, *J. Struct. Geol.*,
486 105, 62-79, <https://doi.org/10.1016/j.jsg.2017.10.011>, 2017.

487 [Malvoisin, B., Austrheim, H., Hetényi, G., Reynes, J., Hermann, J., Baumgartner, L. P. and Podladchikov, Y. Y.:](#)
488 [Sustainable densification of the deep crust, *Geology*, 48, 7, 673-677, <https://doi.org/10.1130/G47201.1>,](#)
489 [2020.](#)

490 McConnell, J.: The origin and characteristics of incommensurate structures in the plagioclase feldspars, *Can.*
491 *Mineral.*, 46, 1389-1400, <https://doi.org/10.3749/canmin.46.6.1389>, 2008.

492 Menegon, L., Stünitz, H., Nasipuri, P., Heilbronner, R. and Svahnberg, H.: Transition from fracturing to viscous
493 flow in granulite facies perthitic feldspar (Lofoten, Norway), *J. Struct. Geol.*, 48, 95-112,
494 <https://doi.org/10.1016/j.jsg.2012.12.004>, 2013.

495 ~~Moore, J., Beinlich, A., Austrheim, H. and Putnis, A.: Stress-orientation dependent reactions during~~
496 ~~metamorphism, *Geology*, 47, 1-4, <https://doi.org/10.1130/G45632.1>, 2019.~~

497 Mukai, H., Austrheim, H., Putnis, C. V., and Putnis, A.: Textural evolution of plagioclase feldspar across a shear
498 zone: Implications for deformation mechanism and rock strength, *J. Petrol.*, 55, 1457-1477,
499 <https://doi.org/10.1093/petrology/egu030>, 2014.

500 Okudaira, T., Shigematsu, N., Harigane, Y., and Yoshida, K.: Grain size reduction due to fracturing and subsequent
501 grain-size-sensitive creep in lower crustal shear zone in the presence of a CO₂-bearing fluid, *J. Struct.*
502 *Geol.*, 95, 171-187, <https://doi.org/10.1016/j.jsg.2016.11.001>, 2016.

503 [Pennacchioni, G., Scambelluri, M., Bestmann, M., Notini, L., Nimis, P., Plümper, O., Faccenda, M. and Nestola,](#)
504 [F.: Record of intermediate-depth subduction seismicity in a dry slab from an exhumed ophiolite, *Earth*](#)
505 [Planet. Sci. Lett., 548, 116490, <https://doi.org/10.1016/j.epsl.2020.116490>, 2020. ~~et al., 2020, EPSL~~](#)

506 Petley-Ragan, A., Dunkel, K. G., Austrheim, H., Ildefonse, B. and Jamtveit, B.: Microstructural records of
507 earthquakes in the lower crust and associated fluid-driven metamorphism in plagioclase-rich granulites.
508 *J. Geophys. Res.-Sol Ea.*, 123, 1-18, <https://doi.org/10.1029/2017JB015348>, 2018.

509 Petley-Ragan, A., Ben-Zion, Y., Austrheim, H., Ildefonse, B., Renard, F. and Jamtveit B.: Dynamic earthquake
510 rupture in the lower crust, *Sci. Adv.*, 5, <https://doi.org/10.1126/sciadv.aaw0913>, 2019.

511 ~~Passehler, C., and Trouw, R.: *Microtectonics*. Springer, Berlin., 2005.~~

512 Reches, Z. and Dewers, T. A.: Gouge formation by dynamic pulverization during earthquake rupture, *Earth Planet.*
513 *Sc. Lett.*, 235, 361-374, <https://doi.org/10.1016/j.epsl.2005.04.009>, 2005.

514 Sharma, S. and Sikka, S.: Pressure Induced Amorphization of Materials, *Progress in Materials Science*, 40, 1-77,
515 1996.

516 Sims, M., Jaret, S. J., Carl, E.-R., Rhymer, B., Schrodte, N., Mohrholz, V., Smith, J., Konopkova, Z., Liermann,
517 H.-P., Glotch, T. D. and Ehm, L.: Pressure-induced amorphization in plagioclase feldspars: A time-
518 resolved powder diffraction study during rapid compression, *Earth Planet Sc. Lett.*, 507, 166-174,
519 <https://doi.org/10.1016/j.epsl.2018.11.038>, 2019.

520 Smith, J. V. and Brown, W. L.: *Feldspar Minerals*, vol. 1, Springer, Berlin, 1988.

521 Soda, Y. and Okudaira, T.: Microstructural evidence for the deep pulverization in a lower crustal meta-anorthosite,
 522 Terra Nova, 1-7, <https://doi.org/10.1111/ter.12355>, 2018.

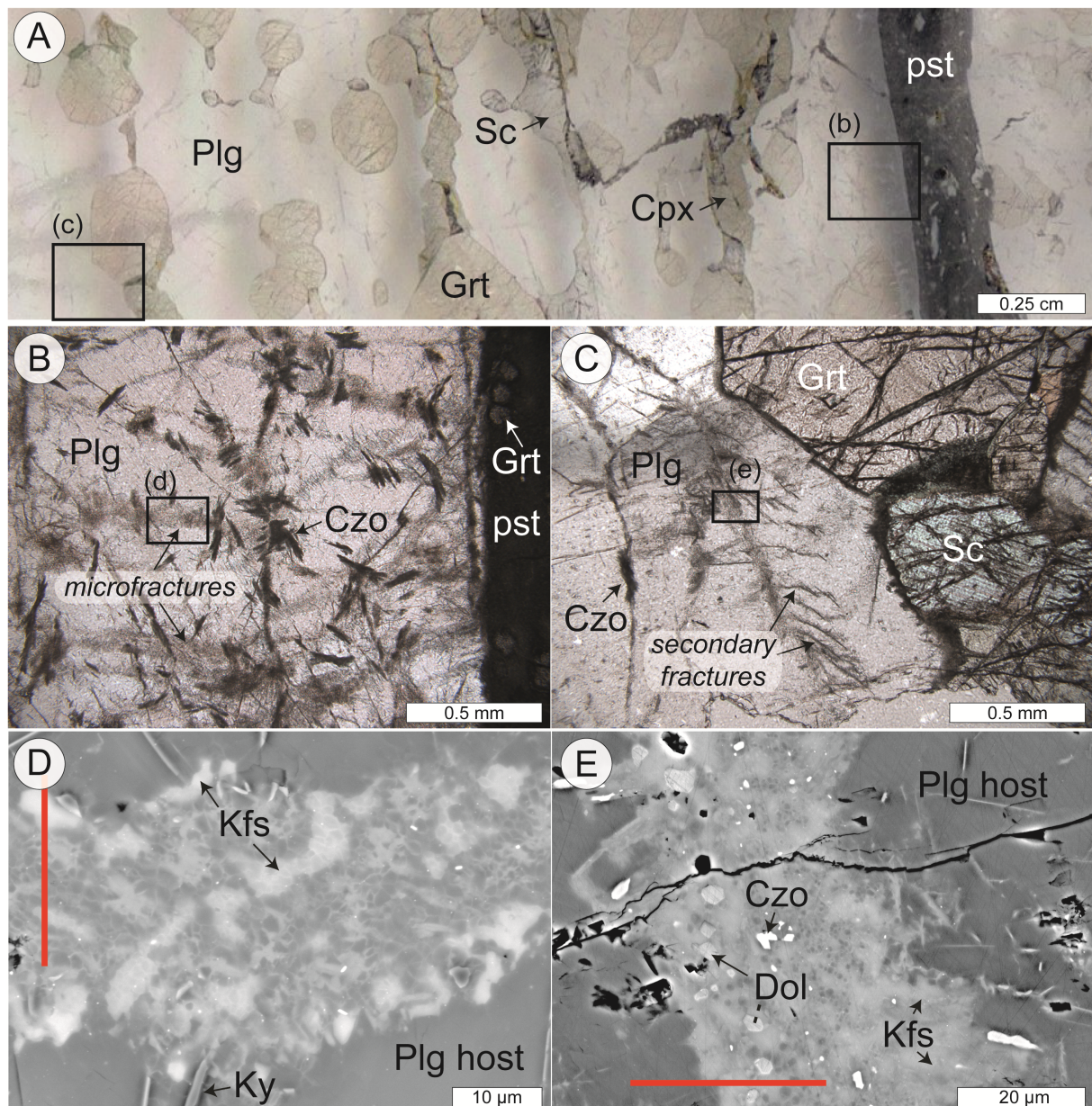
523 Svahnberg, H. and Piazzolo, S.: The initiation of strain localisation in plagioclase-rich rocks: Insights from detailed
 524 microstructural analyses, J. Struct. Geol, 32, 1404-1416, <https://doi.org/10.1016/j.jsg.2010.06.011>, 2010.

525 [Svensen, H., Jamtveit, B., Yardley, B. W. D., Engvik, A. K., Austrheim, H., and Broman, C.: Lead and bromine
 526 enrichment in eclogite facies fluids: Extreme fractionation during lower-crustal hydration, Geology, 27,
 527 467-470, \[https://doi.org/10.1130/0091-7613\\(1999\\)027<0467:LABELIE>2.3.CO;2\]\(https://doi.org/10.1130/0091-7613\(1999\)027<0467:LABELIE>2.3.CO;2\), 1999.](#)

528

529 Tomioka, N., Kondo, H., Kunikata, A. and Nagai, T.: Pressure-induced amorphization of albitic plagioclase in an
 530 externally heated diamond anvil cell, Geophys. Res. Lett., 37, 1-5,
 531 <https://doi.org/10.1029/2010GL044221>, 2010.

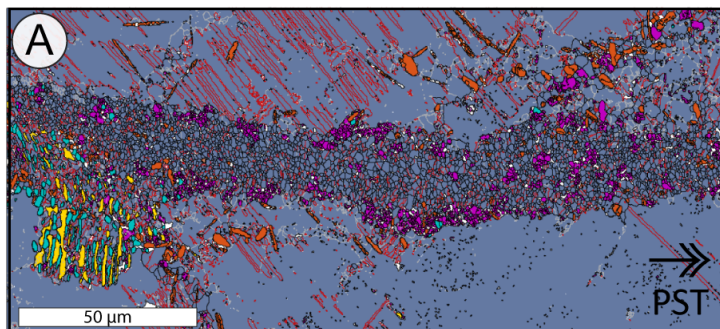
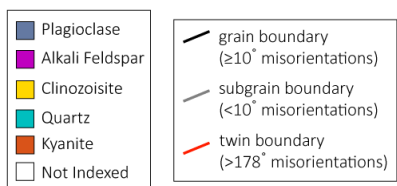
532 Wolf, D., Okamoto, P., Yip, S., Lutsko, J. F. and Kluge, M.: Thermodynamic parallels between solid-state
 533 amorphization and melting, J. Material Res., 5, 286-301, <https://doi.org/10.1557/JMR.1990.0286>, 1990.



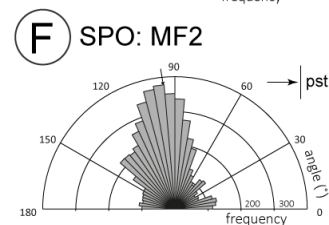
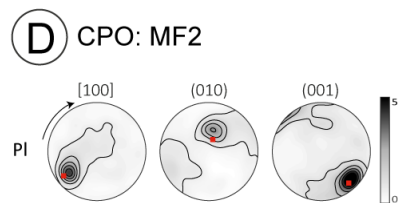
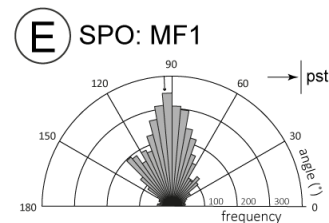
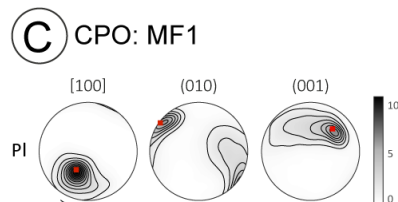
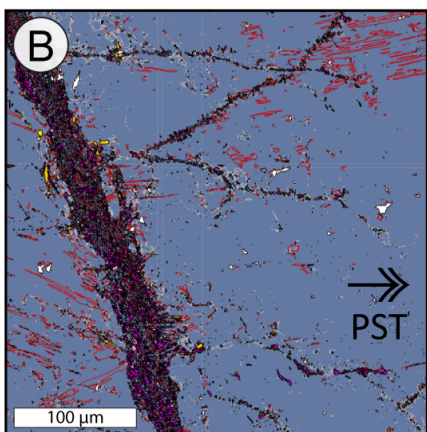
534

535 **Figure 1: Fractured wall rock plagioclase. (a)** Thin section scan of wall rock plagioclase (Plg), garnet (Grt),
536 clinopyroxene (Cpx) and scapolite (Sc) adjacent to an eclogite facies pseudotachylyte (pst) on Holsnøy. **(b)** Fine-
537 grained reaction products of clinozoisite (Czo) are associated with the microfractures. Box denotes the location of
538 MF1. **(c)** Some microfractures in plagioclase display secondary cracking. Box denotes the location of MF2. **(d)**
539 Backscatter electron image of MF1 with fine-grained plagioclase, alkali feldspar (Kfs) and minor kyanite (Ky). **(e)**
540 Backscatter electron image of MF2 with fine-grained plagioclase, K-feldspar, dolomite (Dol) and clinozoisite. Red
541 lines indicate the location of focused ion beam cuts for TEM analysis shown in Figs. 4-6.

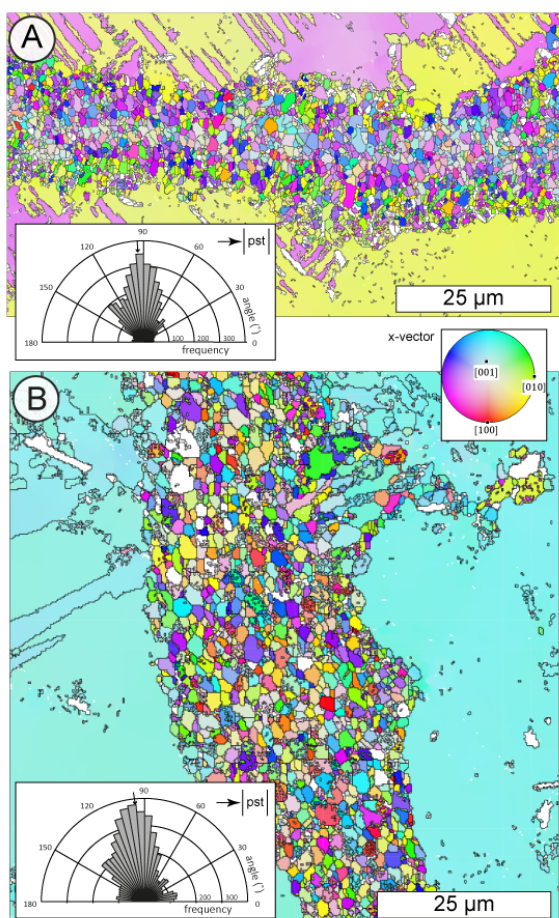
MF1



MF2



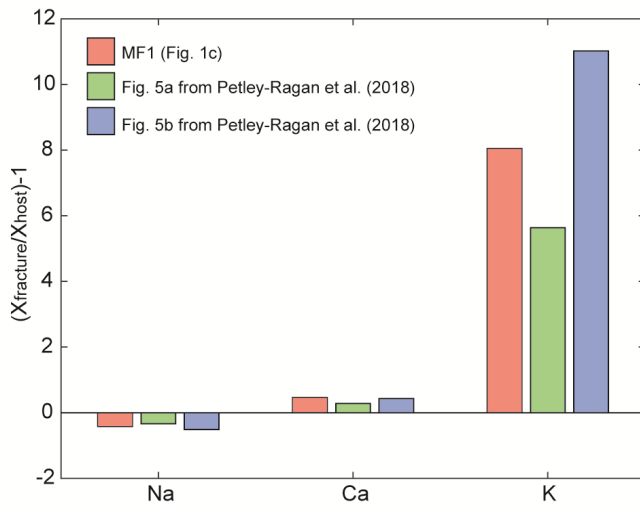
542



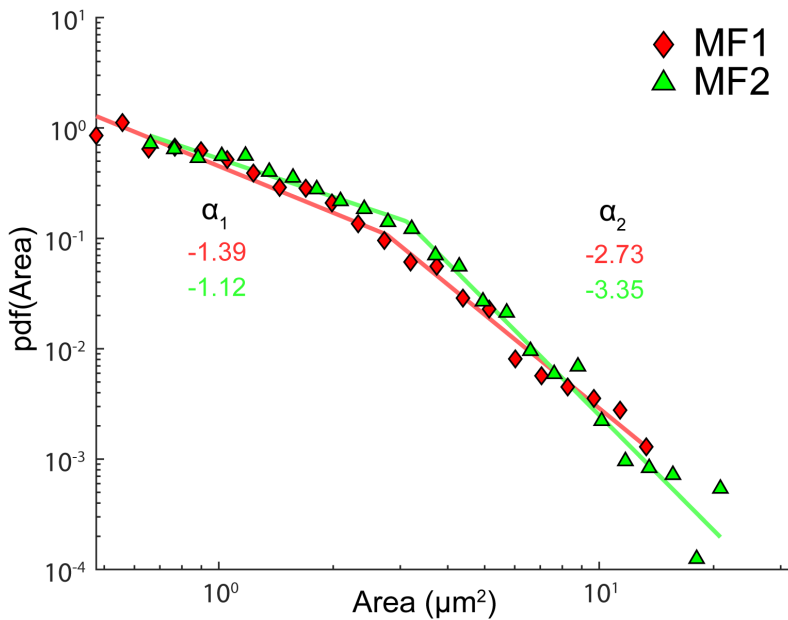
543

544

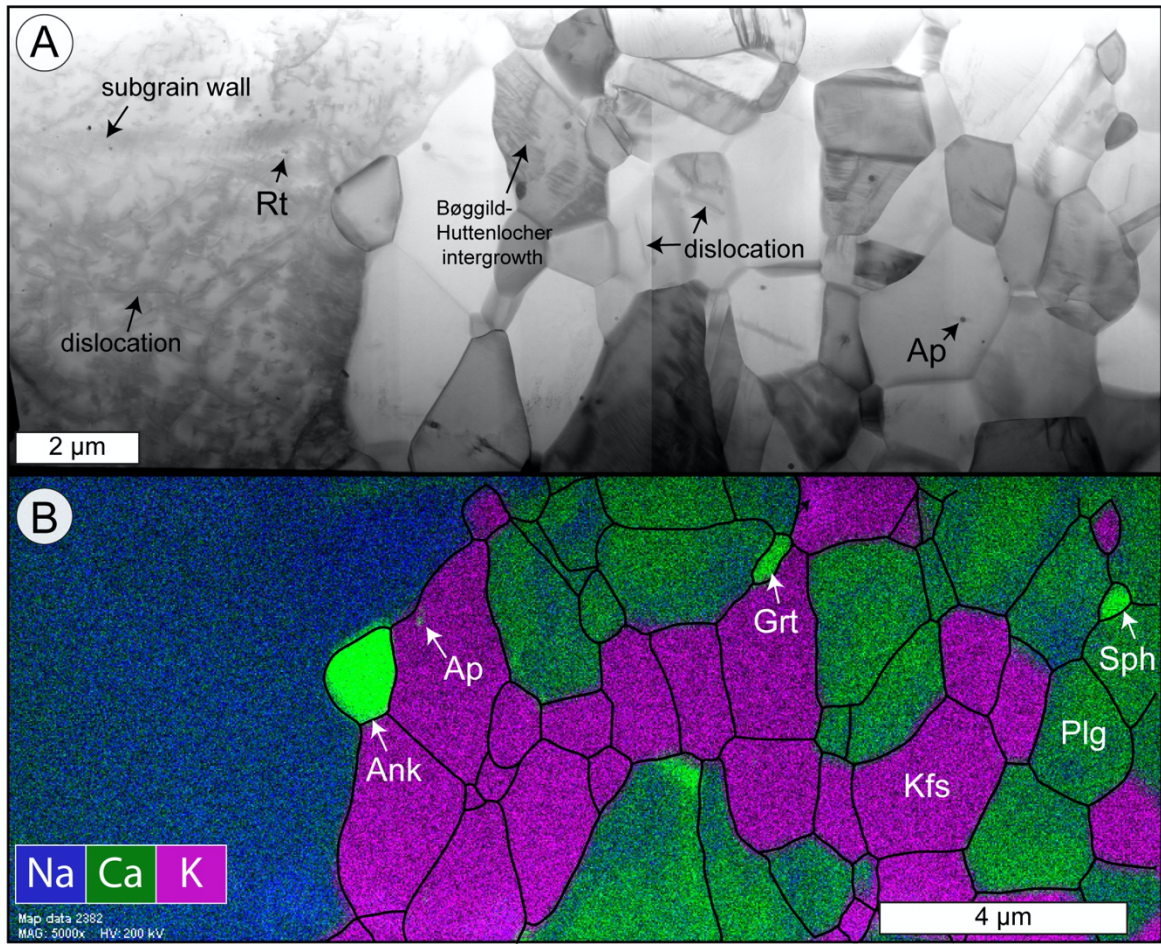
545 **Figure 2: Crystallographic orientations of the grains within the microfractures** EBSD results of MF1 and
 546 **MF2. (a)** Inverse pole figure coloring orientation map of MF1 with inset of grain SPO. **(b)** Orientation map of
 547 **MF2 with inset of grain SPO. Modified after Petley-Ragan et al. (2018).** Phase maps of (a) MF1 and (b) MF2. Pole
 548 **figures of the plagioclase grains in (c) MF1 and (d) MF2. The red dot is the orientation of the host plagioclase.**
 549 **Rose diagrams of the long axis distribution of the plagioclase grains in (e) MF1 and (f) MF2. The pseudotachylyte**
 550 **is to the right of all maps with vertical orientation. See Petley-Ragan et al. (2018) for more details on the EBSD**
 551 **methods and results.**



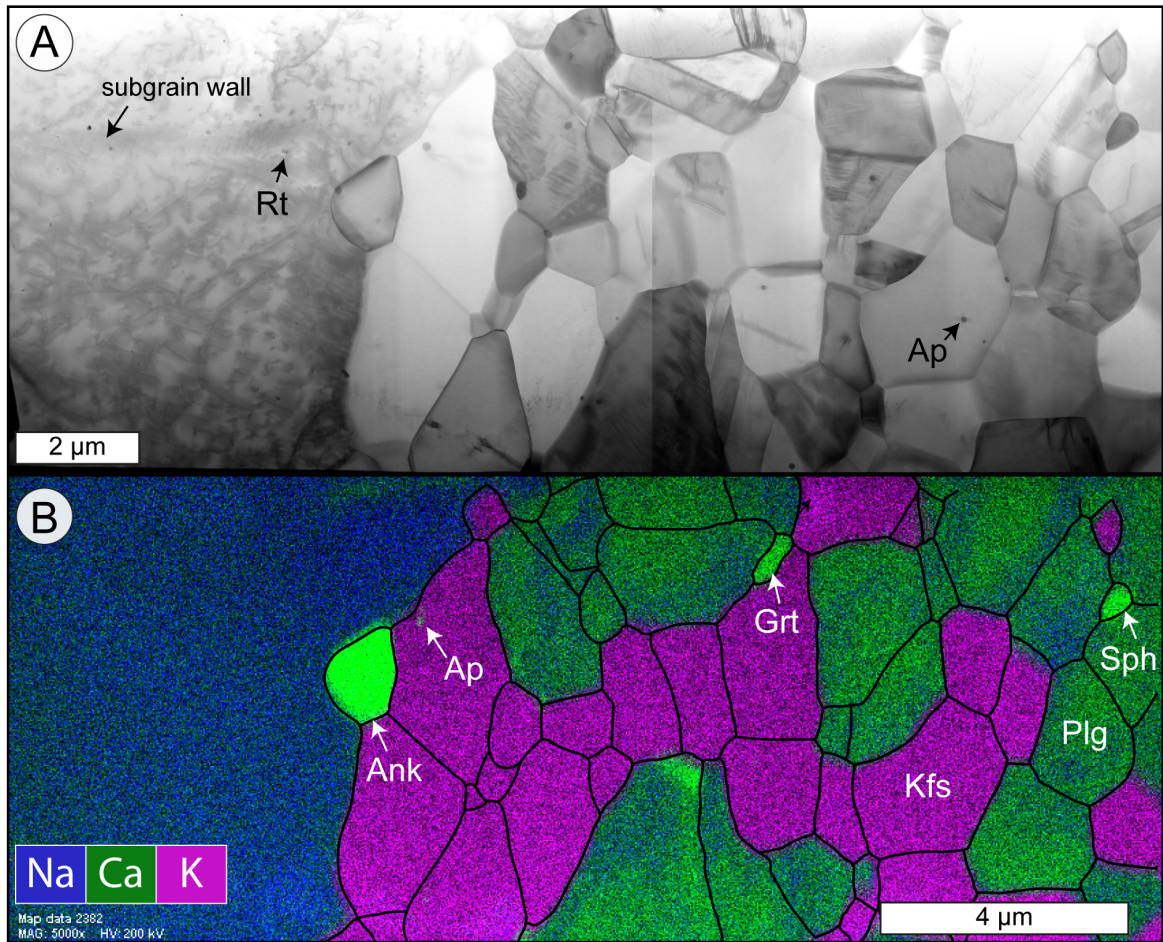
552
 553 **Figure 3: Mass balance of plagioclase microfractures.** Three separate plagioclase microfractures were analyzed
 554 for Na, Ca and K. X_{fracture} is the bulk composition of the fracture and X_{host} is the bulk composition of the adjacent
 555 plagioclase host.



556
 557 **Figure 4: Grain size distribution of plagioclase grains in MF1 and MF2.** A probability density function (pdf)
 558 **was fitted to each distribution. The distributions display two different power law slopes (a) for the small and large**
 559 **grains. See Aupart et al. (2018) for details on the fitting method.**



560



561

562

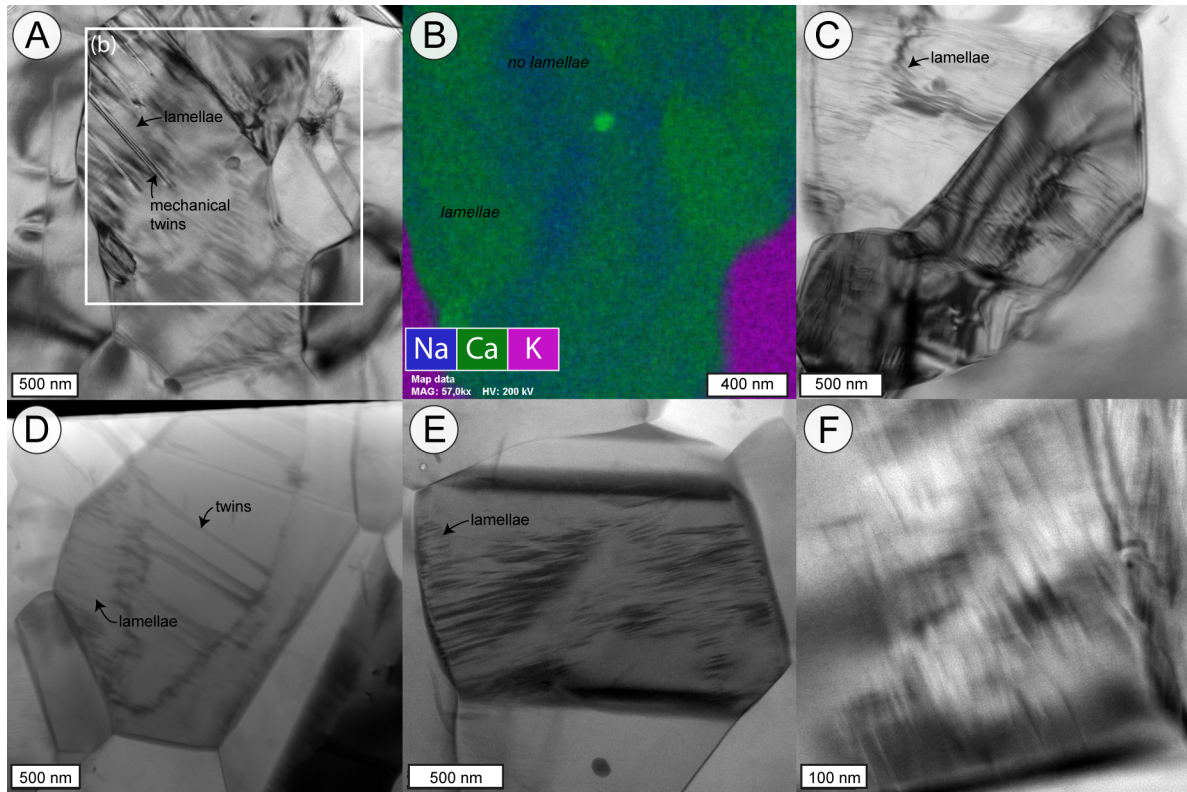
563

564

565

566

Figure 54: Microstructures of MF1. (a) BF-STEM image of the entire FIB cut from Fig. 1d. The plagioclase (Plg) host to the left is rich in dislocations while the grains within the microfracture to the right are poor to absent of dislocations. Apatite (Ap) and rutile (Rt) inclusions are present within the host and the grains, as well as pinned along grain boundaries in the microfracture. **(b)** EDX map overlain with grain and phase boundaries (black). Ankerite (Ank), garnet (Grt) and sphene (Sph) are additional phases within the microfracture.



567

568

569

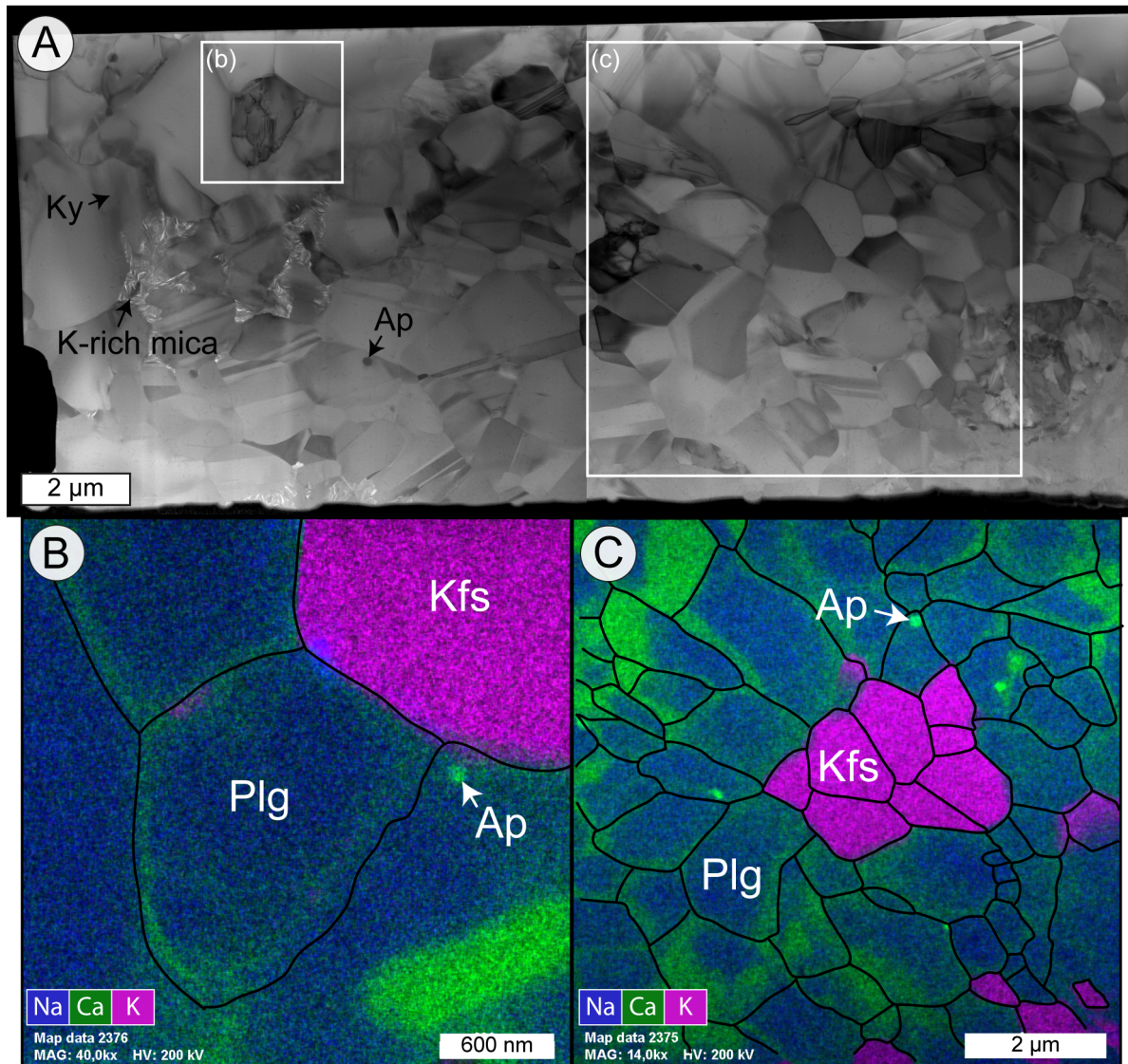
570

571

572

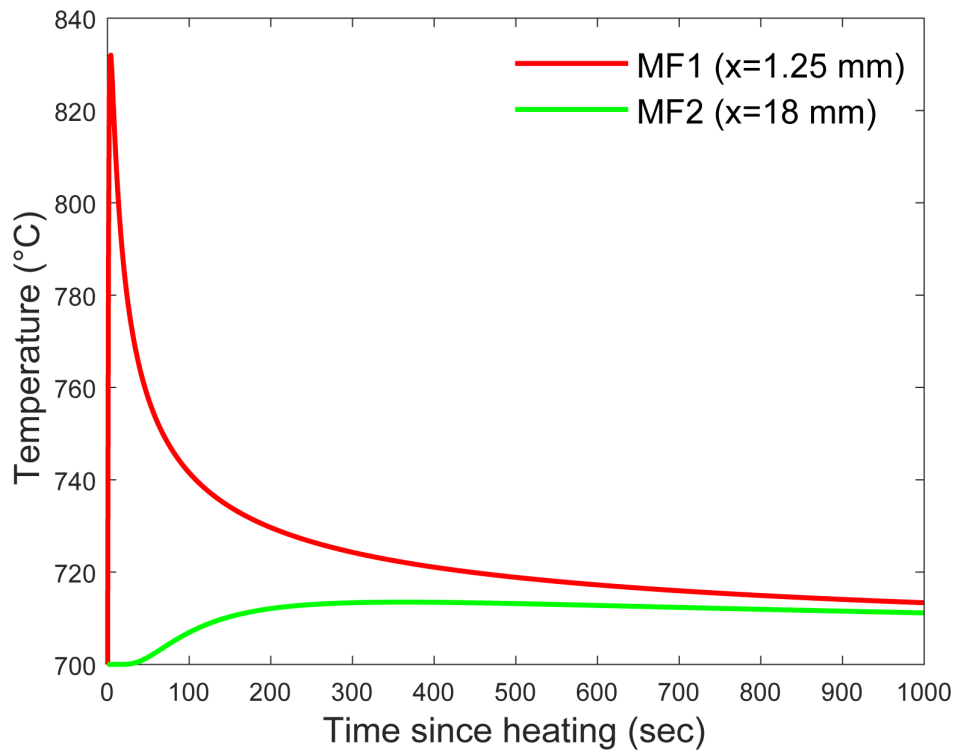
573

Figure 65: Plagioclase intergrowths in MF1. (a) BF-TEM image of the submicron lamellae in a plagioclase grains that are overlain by mechanical twins. (b) EDX map showing the distribution of Ca and Na in the plagioclase grains associated with the intergrowth in (a). The Ca-rich domains overlay the lamellae. (c) BF-TEM image of lamellae in two separate grains that show slight curvature. (d) BF-STEM image of discontinuous lamellae within a grain that hosts twins in its core. (e) STEM bright field image of discontinuous lamellae within a plagioclase grain. (f) Bright field TEM image of lamellae resembling 'tweed' exsolution within plagioclase.



574

575 **Figure 76: Microstructures of MF2.** (a) Bright field image of the entire FIB cut from Fig. 1e. The plagioclase
 576 (Plg) microfracture contains dislocation-free grains with some twins. (b) EDX map of a dislocation-rich grain
 577 overlain with grain and phase boundaries (black). (c) EDX map of the area in (a) overlain with grain and phase
 578 boundaries (black). The Ca-rich domains are present along grain boundaries.



579

580 Figure 8. Results of the steady-state thermal diffusion model. The temperature at each microfracture is
 581 calculated relative to an ambient eclogite facies temperature of 700°C over a timescale of 1000 seconds after
 582 heating up to 1500°C along the fault surface. The heat is considered to first travel through the molten
 583 pseudotachylyte ($k = 0.72 \text{ mm}^2/\text{s}$) before diffusing through the wall rock ($k = 0.48 \text{ mm}^2/\text{s}$). Close to the
 584 pseudotachylyte, MF1 experienced a drastic temperature increase and steep cooling while MF2 experienced only
 585 a slight temperature increase. See results and discussion for details.